FRONTIERS OF PHYSICS

RESEARCH ARTICLE
Volume 21 / Issue 12 / 125204 / 2026

Strain-modulated bulk photovoltaic effect in negative piezoelectrics

Yue Gao[1], Wenli Zou[1], Jian Zhou[2,†], Chunmei Zhang[1,3,‡]

1 School of Physics, Northwest University, Xi'an 710127, China
2 Center for Alloy Innovation and Design, State Key Laboratory for Mechanical Behavior of Materials, Xi'an Jiaotong University, Xi'an 710049, China
3 Shaanxi Key Laboratory for Theoretical Physics Frontiers, Xi'an 710127, China
Corresponding authors. E-mail: †jianzhou@xjtu.edu.cn, ‡chunmeizhang@nwu.edu.cn
Received December 19, 2025; accepted March 27, 2026

© Higher Education Press 2026

ABSTRACT

The bulk photovoltaic effect (BPVE) is mostly studied in ferroelectric and piezoelectric systems with a sizable intrinsic and induced electric dipole moment. While most studies of BPVE are based on the conventional positive piezoelectric materials, their responses in negative piezoelectric systems remain rare. In this work, based on a minimum tight-binding model simulation, we adopt a chain model to illustrate how the BPVE evolves under mechanical deformation in negative piezoelectrics. We find that the BPVE responses are mainly governed by strain-induced shift vector variations. This is in contrast to the conventional positive piezoelectrics. Moreover, such a mechanism is further illustrated in realistic quasi-layered negative piezoelectrics, i.e., rhombohedral GeX (X = S, Se, Te), via density functional theory calculations. Our work provides in-depth insights into BPVE engineering in unconventional negative piezoelectrics.

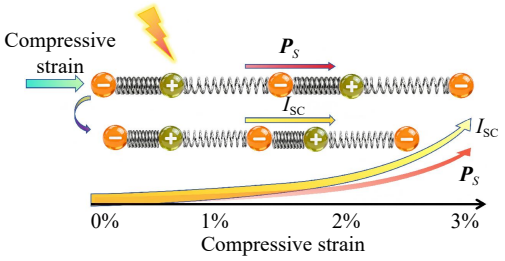

Keywords bulk photovoltaic effect, shift current, negative piezoelectrics, first-principles

1 Introduction

The bulk photovoltaic effect (BPVE) is a nonlinear optical response that enables light-to-electricity conversion [1–4] by generating spontaneous shift and ballistic currents under homogeneous optical illumination [5–9]. The shift current stems from a real space shift in the wave packet center between the valence and conduction bands upon light excitation [10, 11]. It emerges in noncentrosymmetric single phase systems (without requirement of complex heterojunction setup), allowing for overcoming the well-known Shockley–Queisser limit [12], thus offering a novel pathway toward high-efficiency solar cells. Given this, piezoelectrics and ferroelectrics mainly serve as good BPVE platforms. For instance, the first experimental BPVE detection was successfully achieved in ferroelectric $BaTiO_3$, dated back in 1982 [13]. Until recently, BPVE in both piezoelectric and ferroelectric materials have been receiving tremendous attention theoretically and experimentally, owing to their advances of various exotic physical feature under mechanical engineering [14–20], e.g., two-dimensional $CuInP_2S_6$ [14], α-In_2Se_3 monolayer [17], and WS_2 nanotubes [20].

Piezoelectric materials provide a direct interconversion between electrical and mechanical energy [21, 22]. Based on the polarization response to strain along the principal axis, they can be categorized into positive ($\frac{\partial P_i}{\partial \varepsilon_{kl}} > 0$) and negative piezoelectric responses ($\frac{\partial P_i}{\partial \varepsilon_{kl}} < 0$). The vast

https://doi.org/10.15302/frontphys.2026.125204

majority of known piezoelectric materials exhibit positive piezoelectricity. Their BPVE enhances concurrently with increasing polarization under tensile strain, such as in SnS [23], and 2H/3R-MoS_2 [24, 25]. In contrast, studies on negative piezoelectric materials remain relatively nascent [26–29]. Furthermore, we note that mechanical strain engineering provides an effective means for modulating the photovoltaic effect [30, 31], while their distinct strain-polarization response would lead to different BPVE behavior compared with the positive piezoelectric materials [15]. These materials have emerged as a pivotal platform for realizing and studying the negative piezoelectric effect [28, 29] due to their pronounced structural anisotropy and unique polarization rotation mechanisms.

In this work, we employ a one-dimensional (1D) minimum model to simulate the BPVE in negative piezoelectric platforms, adopting a tight-binding (TB) model calculation. Our calculations reveal that a uniaxial tensile (compressive) strain along the spontaneous polarization axis could suppress (enhance) the shift vector. It furthermore modulates the BPVE, especially the shift current conductivity. In addition, we perform first-principles density functional theory (DFT) calculations to evaluate the BPVE in rhombohedral GeX (X = S, Se, Te) compounds, which exhibit a large negative longitudinal piezoelectric coefficient. Our calculations reveal a significant shift current photoconductance of 164 μA/V^2 at 0.8 eV under a 3% compressive strain along the [001] direction of the conventional cell (or the [111] direction of the primitive cell), surpassing most ferroelectric materials.

2 Computational details

All first-principles calculations in this study employ the Vienna *ab initio* simulation package (VASP) based on DFT [32]. We treat exchange–correlation interactions using the generalized gradient approximation (GGA) using the Perdew–Burke–Ernzerhof (PBE) form [33], and the core-valence electron interactions are computed via the projector augmented-wave (PAW) method [34]. Valence electrons are expanded using a plane-wave basis set with a 500 eV kinetic energy cutoff to ensure electronic accuracy. The first BZ of the conventional unit cell is sampled using the Γ-centered Monkhorst–Pack k-meshes with a grid of 15 × 15 × 5 [35]. For structural relaxation, the convergence criteria for total energy and force component are set as 1 × 10^{-6} eV and 0.001 eV/Å, respectively. Modern theory of polarization is used to calculate the electron contributed electric polarization along the periodic boundary [36]. The shift current photoconductances are computed via the maximally localized Wannier functions (MLWFs) using the WANNIER90 package [37, 38]. We employ a refined 300 × 300 × 150 k-point mesh and a 0.04 eV delta-function broadening to yield converged shift current components. The spin–orbit coupling (SOC) is included self-consistently throughout all the calculations.

3 Simplified low-energy model

We begin with a simple 1D model with two ions in a unit cell. The formal charges of them are denoted as $\pm Z$. At the equilibrium structure, their interatomic bond distances are denoted as R_1 and R_2, with the lattice constant of $L = R_1 + R_2$ [as illustrated in Fig. 1(a)]. To simulate their ionic interactions, we adopt a spring-like potential for the alternative bonds, described by spring stiffness coefficients k_1 and k_2, respectively. This structure is similar to the well-known Su–Schrieffer–Heeger model [39] to describe the polyacetylene. Since the electric dipole moment in a periodic boundary condition is ill-defined, we follow the conventional approaches to denote that when $R_1 = R_2$, the total spontaneous polarization $P = 0$. This is the referenced state. Under a nonzero distance mismatch $\eta = R_2 - R_1 \neq 0$, net polarization occurs, which is contributed from ionic and electronic parts separately. In the following, we break down their contributions and estimate their effects on the sign of the piezoelectric coefficient $d = \frac{\delta P}{\delta \varepsilon}$. Here, ε represents a uniaxial strain along the chain, defined as $\varepsilon = \frac{L' - L}{L}$.

The ionic part contribution is $P_{\text{ion}} = \frac{Z\eta}{2L}$. Under finite strain, the new lattice constant is $L' = R_1' + R_2'$. At such a new equilibrium structure, it is clearly that $\frac{R_1' - R_1}{R_2' - R_2} = \frac{k_2}{k_1}$. Hence, we can estimate the piezoelectric constant as

$$d_{\text{ion}} = \frac{\delta P_{\text{ion}}}{\delta \varepsilon} = \frac{Z}{(k_1 + k_2)\, L'} \left(R_1 k_1 - R_2 k_2\right). \tag{1}$$

Therefore, the sign of $\frac{\delta P_{\text{ion}}}{\delta \varepsilon}$ is determined by two factors, the formal charge Z and the relative magnitude between equilibrium distance $\frac{R_2}{R_1}$ and stiffness $\frac{k_1}{k_2}$. One also observes that the piezoelectric coefficient d_{ion} is inversely proportional to strained lattice constant L', which gives a nonlinear $P_{\text{ion}} - \varepsilon$ relationship. We plot the diagram of polarization change with respect to strain ε and $Z\left(\frac{k_1}{k_2} - \frac{R_2}{R_1}\right)$ in Fig. 1(b).

Next, we discuss the electronic polarization P_{el}. We adopt a two-orbital spinless tight-binding model

$$H = -\frac{t}{2}\sum\nolimits_n \left(c_n^\dagger c_{n+1} + c_{n-1}^\dagger c_n\right) + \frac{\Delta}{2}\sum\nolimits_n (-1)^i c_n^\dagger c_n. \tag{2}$$

Here, t is the hopping integral between nearest neighbor ions, and $\pm\frac{\Delta}{2}$ is their on-site energies. We focus on semiconductors with large on-site energy difference than the hopping parameter, namely, $\beta = \left|\frac{t}{\Delta}\right| \ll 1$. The eigenenergies take the form of $E_\pm(k) \simeq \pm\frac{\Delta}{2}\left(1 + 8\beta^2 \cos^2 \frac{kL}{2}\right)$. It opens a direct band gap at the Brillouin zone boundary

$k = \pm\frac{\pi}{L}$. The valence band Bloch wave function is

$$|u_-(k)\rangle = \frac{1}{\sqrt{N_-(k)}}\begin{pmatrix} -\beta g(k)\,\Delta \\ \frac{\Delta}{2}\left(1+\sqrt{1+4\beta^2|g(k)|^2}\right)\end{pmatrix}, \tag{3}$$

where $g(k) = 2e^{i\frac{\eta}{2}k}\cos\frac{Lk}{2}$, and $\sqrt{N_-(k)}$ is the normalization factor. With this wavefunction, we can evaluate the electron contributed polarization according to the Berry phase theory [36],

$$P_{\text{el}} = -\beta^2\frac{e\eta}{L} + O\left(\beta^3\right). \tag{4}$$

Here, we expand the expression according to the power of the unit-free parameter β. One sees that the polarization is zero when the two sites are equally separated ($\eta = 0$), consistent with the previous assumption. Since $P_{\text{el}} \propto \frac{1}{L}$, the tensile (compressive) strain could reduce (enhance) the magnitude of $|P_{\text{el}}|$. Performing derivative, we have $d_{\text{el}} = \frac{\delta P_{\text{el}}}{\delta\varepsilon} = \frac{-2\beta^2 e}{(k_1+k_2)L^r}(R_1k_1 - R_2k_2)$, also determined by the relative magnitude between equilibrium distance $\frac{R_2}{R_1}$ and stiffness $\frac{k_1}{k_2}$. Note that we assume a constant hopping integral t in the model, based on the small strain deformation approximation. Nevertheless, as $P_{\text{el}} \propto \beta^2$, the electron contributed polarization (and the piezoelectric coefficient) is orders of magnitude smaller than the ion contributions P_{ion}. The detailed derivations of both electric and ionic polarization are given in Supporting Information.

Without loss of generality, we assume $Z > 0$, then such a model describes negative piezoelectric feature under condition of $k_1\frac{R_1}{R_2} < k_2 < k_1$. Building upon the reported negative piezoelectric materials [28, 29], we select appropriate atomic distances for this model. Meanwhile, within the reasonable parameter range defined by this criterion, we select a representative set of k_1 and k_2 coefficients to derive distinct TB parameters for negative piezoelectric effects, as detailed in Supporting Information. Taking parameters of $\Delta = 1$, the direct band gap E_g opens at the X point with a value of 1.0 eV at the equilibrium structure [Fig. 1(c)]. Based on the above conditions, the total electric polarization increases under compressive strains (ε = –2%–0%) [Fig. 1(d) and Table S1]. Opposite behaviors emerge under tensile strains (ε = 0%–2%).

To investigate the BPVE in negative piezoelectrics, we evaluate the shift current in this 1D chain model. The shift current photoconductance $\sigma^{aaa}(\omega)$ under linearly polarized light (LPL, polarized along a) is evaluated by [41, 42]

$$\sigma^{aaa}(\omega) = \frac{\pi e^3}{\hbar^2}\int\frac{\mathrm{d}k}{2\pi}\sum_{m,n} f_{n,m}R^{a,a}_{mn}|r^a_{mn}|^2\delta(\omega_{nm}-\omega), \tag{5}$$

where a is the longitudinal direction. $f_{n,m} = f(E_n) - f(E_m)$ is the difference of Fermi–Dirac occupation (m and n are the band indices). $r^a_{mn} = \mathrm{i}\langle m|\partial_{k_a} n\rangle$ is the interband Berry connection. The shift vector is defined as $R^{a,a}_{mn} = \partial_a\phi^a_{mn} - \mathcal{A}^a_{mm} + \mathcal{A}^a_{nn}$, where $\mathcal{A}^a_{mm}$ is intraband Berry connection and ϕ^a_{mn} is the phase of $r^a_{mn} = |r^a_{mn}|\,e^{i\phi^a_{mn}}$. The shift vector represents the positional change of a wave packet during the transition from the n^{th} to the m^{th} band. The $|r^a_{mn}|^2\delta(\omega_{nm}-\omega)$ measures the absorption rate according to the Fermi's golden rule. All quantities are $\boldsymbol{k}$-dependent.

The 1D chain can generate a shift current tensor σ^{xxx} along the extended direction. As shown in Fig. 1(e), the shift current of the 1D chain exhibits the largest σ^{xxx} peak at the photon energy of about 1.0 eV, primarily contributed by the electronic transitions between the valence band maximum (VBM) and conduction band minimum (CBM) near the X point. Note that in evaluating shift current variation with strain, we assume the hopping parameter t changes with bond length. Thus, bandgap E_g changes with strain, which is demonstrated in Supporting Information. One observes that the shift current increases under compressive strains, whereas it decreases under tensile strains [Fig. 1(e) and Table S1]. When strains are applied, the bandgap remains nearly unchanged, indicating that the bandgap-dominated absorption is not the primary mechanism responsible for the variation of shift current. In order to elucidate the origin of such a σ^{xxx} variation, we further calculate the shift vector between valence and conduction band (R_{vc}). Its variation at the X point under different ε is shown in Fig. 1(f), which is monotonously increased (reduced) under compression (tension). This suggests that the shift vector is responsible for shift current modulations. Note that the shift vector represents the displacement between Wannier wavepacket centers during electron excitation from the valence to conduction bands, which can be well-modulated under the strain. Furthermore, a parallel conclusion is conducted with respect to positive piezoelectric systems according to the 1D chain model – tensile strain concurrently increases polarization and shift current (details can be found in Supporting Information Fig. S1 and Table S2), which aligns with the BPV mechanisms of positive piezoelectric materials previously [23–25]. The variation of shift current in negative piezoelectric materials is fundamentally different from that in conventional positive piezoelectric materials under strains, as exemplified in Table S3.

4 Realistic materials of rhombohedral GeTe

We then perform DFT calculations to illustrate our discussions in a realistic material, r-GeTe, which exhibits sizable nonlinear optical responses [42–44].

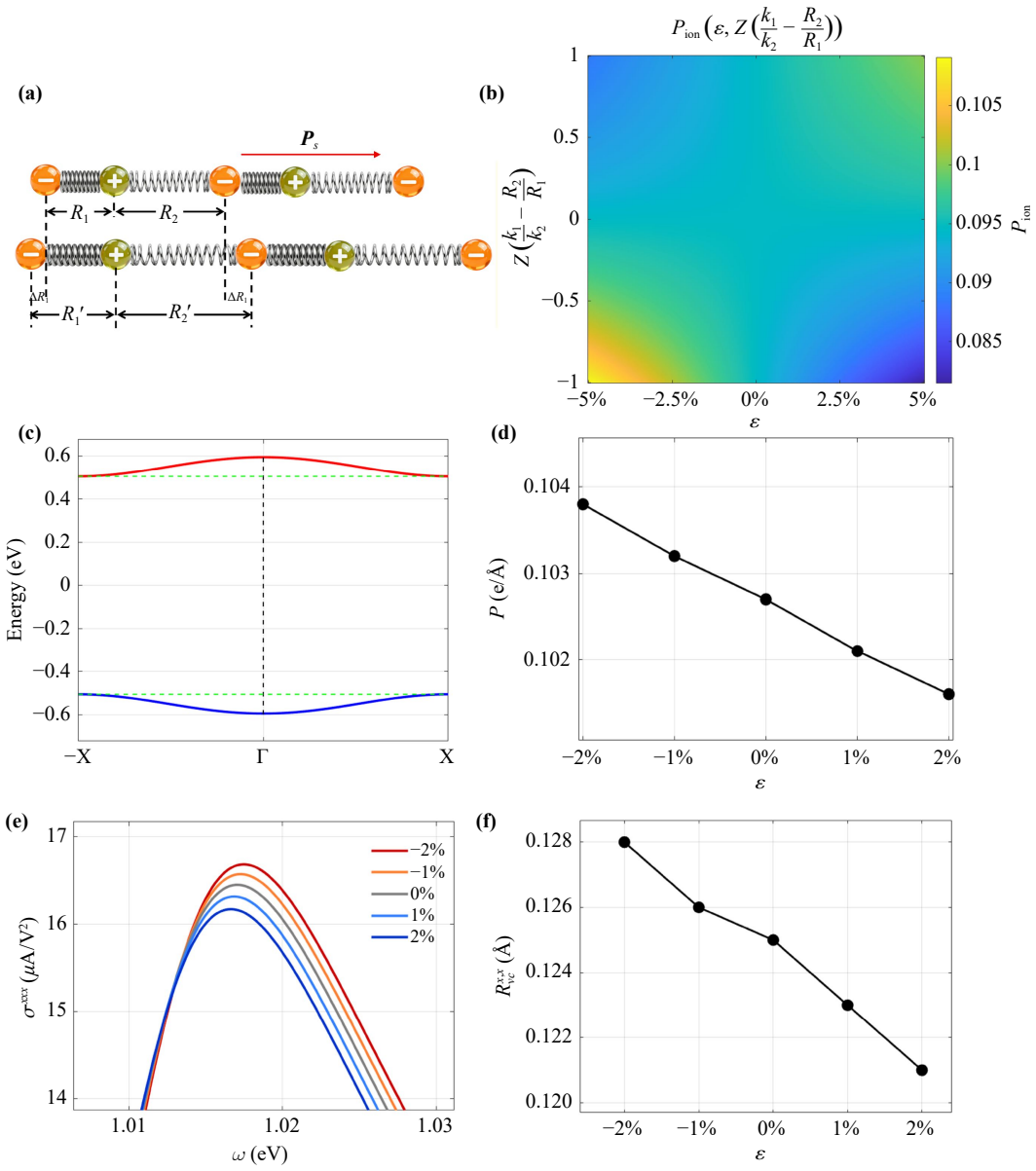

Fig. 1 **(a)** A simplified 1D model for the negative piezoelectric effect in materials. The green and orange balls represent positive and negative ions, respectively. The red arrows indicate the spontaneous polarization direction. **(b)** Diagram of polarization change with respect to strain ε and $Z\left(\frac{k_1}{k_2}-\frac{R_2}{R_1}\right)$. **(c)** Tight-binding model calculated the energy band of a 1D chain at the equilibrium structure. The Fermi level is set to be 0 eV. **(d)** The variation of polarization for the 1D chain TB model under strain (ε = −2% – +2%) in the negative piezoelectric regime. **(e)** The shift current, and **(f)** shift vector at X points of the 1D chain TB model under strain in the negative piezoelectric regime.

Especially, r-GeTe is a "quasi-layered" material with pronounced negative longitudinal piezoelectric coefficients (d_{33} = −70.87 pC/N) [30]. Given these attributes, we leverage layered ferroelectric r-GeTe as an ideal platform for investigating the BPVE mechanism under negative piezoelectric responses. Below $T_C \approx 720$ K, r-GeTe exhibits a non-centrosymmetric structure with space group of $R3m$ (No. 160) [Figs. 2(a, b)]. We take the conventional hexagonal unit cell [Fig. 2(c)], which is composed of three Ge atoms and three Te atoms alternately arranged along the z-axis, with unequal "stiff" (d_1) and "soft" (d_2) interlayer regions [29]. The short and long Ge–Te bonds are optimized to be 2.856 Å and 3.255 Å, respectively. The Ge–Te bond lengths corresponding to the shorter d_1 region and the longer d_2 region are 1.482 Å and 2.153 Å, respectively. The optimized lattice constants of r-GeTe are $a = b = 4.228$ Å and $c = 10.902$ Å, which are consistent with previous theoretical and experimental studies [29, 45].

The calculated electronic band dispersion in the first Brillouin zone [Fig. 2(d)] is shown in Fig. 2(e). The electronic structure calculations reveal an indirect bandgap

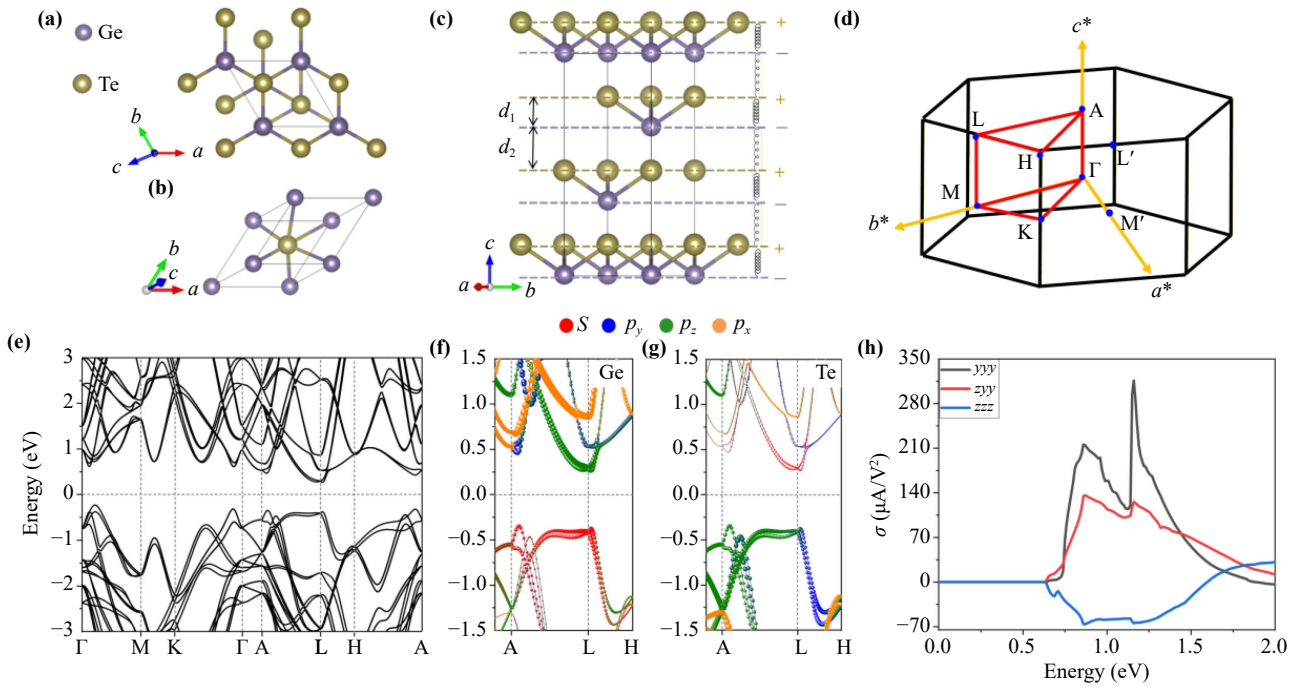

Fig. 2 **(a)** Top and **(b)** aerial views of crystal structures of primitive cells for r-GeTe. **(c)** The side view of the conventional cell. **(d)** The first Brillouin zone (BZ). **(e)** Energy band structure with SOC. **(f, g)** The orbital-resolved band structure for Ge and Te atoms. **(h)** Shift current photoconductance of the bulk r-GeTe.

of 0.64 eV without SOC for r-GeTe [Fig. S2], which agrees well with previous studies [46–48]. Inclusion of SOC activates a Rashba-like spin splitting in the vicinity of the L (and its equivalent) point [Fig. 2(e)], which reduces the band gap to 0.50 eV. Orbital-projected bands [Figs. 2(f, g)] confirm that the VBM (near the L point) is dominated by the Ge-s, Te-p_y, and p_z orbitals, and the CBM is mainly formed by the hybridization of the Te-s, and Ge-p_z, orbitals. Notably, the difference between Te-p_x and p_y orbitals contributions reflects the reduced crystal symmetry and the use of a fixed global Cartesian basis in the orbital projection, rather than a physical inequivalence of the electronic states.

Then, we evaluate the shift current of the bulk r-GeTe. The r-GeTe displays a C_{3v} point group symmetry, allowing two independent out-of-plane shift current response tensors ($\sigma^{zyy} = \sigma^{zxx}$, σ^{zzz}) and the M_x reflection operation allows only one independent in-plane photoconductance tensor component. Figure 2(h) shows the shift current photoconductivity, which is consistent with previous results [36]. One sees that σ^{yyy}, σ^{zyy}, and σ^{zzz} all exhibit sizable shift current at their first peak with photon energy of 0.87 eV [Fig. 2(h)], with their peak values of 219 μA/V^2, 137 μA/V^2, and 66 μA/V^2, respectively. The k-resolved shift current in the first BZ [Figs. S3(a)–(f)] reveals that the first peak values of σ^{yyy} and σ^{zyy} are contributed by electron hopping around the A, and L′ points. The σ^{zzz} is primarily contributed by electron transitions around the L (and L′) point. Critically, orbital-projected bands [Figs. 2(f, g)] show these electronic transitions are mediated by interlayer Ge and Te orbitals hybridization, closely linking shift current generation to anisotropic bonding in the quasi-layered structure. We further calculate the resolved contribution of the shift currents from the Ge and Te atomic layers [49, 50]. The nearly equal quasi-layer-resolved shift-current contributions [Fig. S4] suggest that the BPVE in r-GeTe originates from electronic transitions between the strong interlayer Ge–Te orbital hybridization.

To investigate the shift current variation under strain, we systematically modulate ε in the range of –3% to 3% along the z-axis. Here, $\varepsilon = (c - c_0)/c_0$ represents the uniaxial strain applied along the z-axis, where c_0 and c denote the lattice constants along the z direction of the hexagonal unit cell at the equilibrium state and under deformation, respectively. The two inequivalent interlayer regions in r-GeTe respond differently under strain [Fig. 3(a)]. In detail, we find that tensile (compressive) strain expands (contracts) the interlayer distance (d_2), while the d_1 remains nearly unchanged. This structural distortion directly modulates net electric dipoles formed by alternating Ge and Te atomic layers. Consequently, the calculated polarization along the z-direction decreases (increases) under tensile (compressive) strain, exhibiting a negative longitudinal piezoelectric response, consistent with previous works [29]. Furthermore, the bandgap variation (ΔE_g = –0.047 – +0.024 eV) does not change too much within the deformation regime [Fig. 3(b)], which indicates a weak correlation with respect to the shift current conductance modulation.

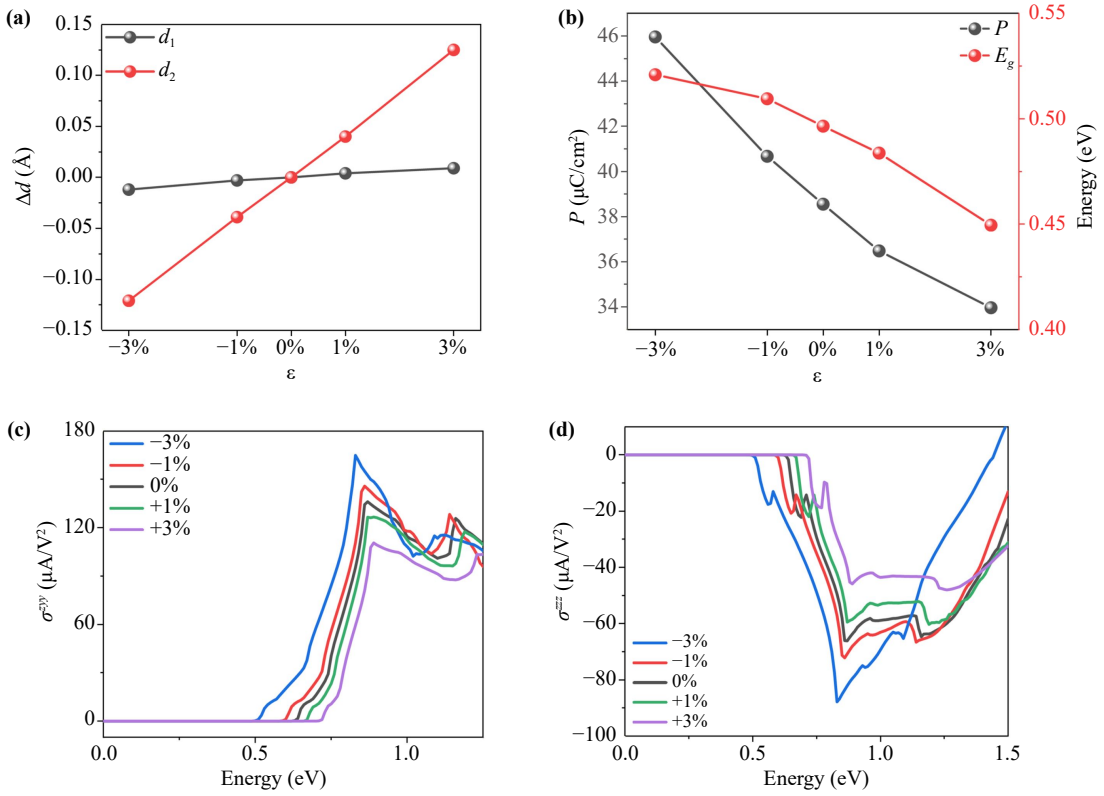

Fig. 3 **(a)** Interlayer distances d_1 and d_2 variation, **(b)** electric polarization and bandgap, shift current conductance **(c)** $\sigma^{zyy}(\omega)$ and **(d)** $\sigma^{zzz}(\omega)$ of the bulk r-GeTe under strain.

The mechanical deformation induced changes of shift current photoconductance (σ^{zyy} and σ^{zzz}) are plotted in Figs. 3(c, d). One sees that the out-of-plane shift current components σ^{zyy} and σ^{zzz} exhibit significant enhancement under compressive strains and reduction under tensile strains [Figs. 3(c, d)], in agreement with the polarization variation [Fig. 3(b)]. This trend is primarily driven by strain-induced shift vector modifications [as plotted in Fig. S5], aligns with the physical picture proposed in the simplified 1D model. Specifically, compressive strain significantly reduces the "soft" d_2 interlayer regions, enhancing the Ge-p_z and Te-p_z orbital hybridization at the VBM, as shown in Table S4. This hybridization increases both the polarization and the interband Berry connection [Fig. S6]. Their simultaneous effects lead to an enhanced shift current. Moreover, the in-plane shift current tensor σ^{yyy} exhibits much less variations under ε [Fig. S7]. Furthermore, we find that all shift current conductance components under in-plane biaxial strain exhibit no discernible changes [Fig. S8].

Besides, at ε = –3%, the σ^{zyy} and σ^{zzz} of r-GeTe increase to 164 μA/V^2 and –87 μA/V^2 at ω = 0.8 eV, respectively. The shift current peak values surpass those of the previously reported ferroelectric materials: the shift current of σ^{zxx}~0.8 μA/V^2 (at ω = 3.8 eV) in the multiferroic material $BiFeO_3$ [51], σ^{zzz}~50 μA/V^2 (at ω = 6.0 eV), σ^{zzz}~30 μA/V^2 (at ω = 6.5 eV) in the prototypical ferroelectrics $PbTiO_3$, and $BaTiO_3$ [52], and σ^{yxx}~100 μA/V^2 in the As monolayer (at ω = 0.18 eV) [15].

To explore the universality of strain-modulated BPVE in piezoelectric systems, we investigate other Ge chalcogenides r-GeS (–140.67 pC/N) and r-GeSe (–71.45 pC/N) [30]. Both rhombohedral GeS and GeSe belong to the *R*3*m* space group, and exhibit sizable shift current conductance σ^{yyy}, σ^{zyy}, and σ^{zzz} [Fig. S9]. In the presence of SOC, GeS and GeSe are semiconductors with indirect bandgaps of 0.50 eV and 0.47 eV [Figs. 4(a, b)], respectively. One sees that the strain-dependent bandgap evolution in GeX (X = S, Se, Te) is different [Fig. 4(c)], attributed to the chalcogen-dependent orbital compositions and deformation potentials at the band edges. Figs. 4(d, e) show the first peak value of σ^{zyy} and σ^{zzz} of r-GeS and r-GeSe under an out-of-plane strain. Similarly, one sees that compressive (tensile) strain enhances (reduces) the σ^{zyy} and σ^{zzz} of the r-GeS and r-GeSe. Here, we report the peak value change (with referenced to the strain-free state) $\Delta\sigma^{zaa} = \sigma^{zaa}(\varepsilon) - \sigma^{zaa}(\varepsilon = 0)$ $(a = y, z)$ of each structure. The variation of shift current reflects the inherent strain-driven polarization response in negative longitudinal piezoelectric materials, thereby establishing it as a strategy to probe the polarization.

Our simplified 1D chain model and DFT calculations

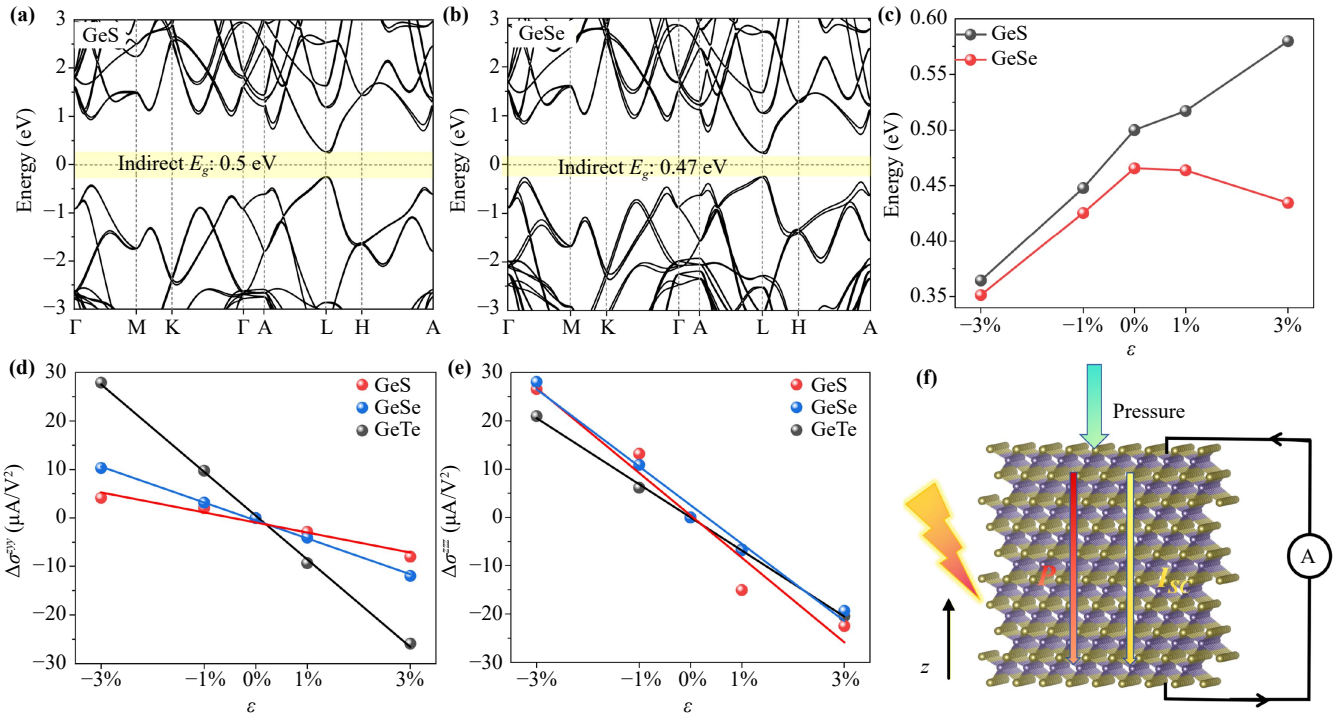

Fig. 4 Calculated band structure with SOC of **(a)** GeS and **(b)** GeSe. **(c)** The bandgap of GeS and GeSe. The first peak value change of shift current conductance of **(d)** $\Delta\sigma^{zyy}$ and **(e)** $\Delta\sigma^{zzz}$ of bulk r-GeX (X = Te, S, Se) under different strains, as compared to their corresponding strain-free results. **(f)** The schematic diagram of pressure-driven infrared photodetector based on the ferroelectric r-GeX.

establish the strain-modulated shift current as a ubiquitous feature of negative piezoelectric materials, arising from the strain-modulated shift vector. Within the framework of the modern theory of polarization, the electric polarization P is directly determined by the spatial distribution of Wannier centers of the occupied bands, such that changes in polarization essentially correspond to the collective displacement of Wannier centers. Meanwhile, the shift vector measures the displacement between Wannier centers during electron excitation from the valence to conduction bands. Consequently, mechanical strain provides an effective means to tune the shift vector, thereby governing the shift current conductance variation in negative piezoelectric materials. We note that similar strain-modulated BPVE behaviors have also been reported in other negative piezoelectric systems. For instance, As/Bi monolayer with negative longitudinal piezoelectric coefficients [53] exhibits a pronounced enhancement of shift current under compressive strain [15]. Overall, our study offers a viable strategy for mechanically modulating the BPVE in negative piezoelectric materials.

Based on our previous prediction that strain can effectively modulate the BPVE in negative piezoelectric materials, we propose that negative longitudinal piezoelectric GeX (X = S, Se, Te) can be utilized to construct a pressure-tunable infrared photodetector, as illustrated in Fig. 4(e). Unlike conventional infrared detectors that rely on an external bias, the device generates a sizable shift current under infrared illumination, enabling self-powered, zero-bias, and high-sensitivity infrared detection. Notably, both the sensitivity and response speed of the photodetector can be tuned via compressive strain, enabling multilevel photoconductance. The estimated responsivity of a GeTe-based photodetector can be tuned approximately 0.123 A/W around 0.8 eV with an optical alternating electric field magnitude of 0.01 V/nm (a moderate strength within the experimental achievable regime), comparable with the 0.191 A/W reported for a BPVE-based self-powered MoS_2 device [54].

5 Conclusion

In summary, we unravel a ubiquitous strain-modulated shift current response mechanism in negative piezoelectric materials. We adopt a TB model and reveal that compressive strain along the spontaneous polarization direction could simultaneously enhance the shift current and polarization. This contrasts with the positive piezoelectric systems, mainly stemming from the distinct strain-driven shift vector modifications. We would like to note that the BPVE could exist in piezoelectrics at the equilibrium state, while our study mainly focuses on its engineering. Furthermore, we illustrate this mechanism using r-GeX (X = S, Se, Te) according to first-principles

calculations. The out-of-plane shift current conductance components σ^{zyy} and σ^{zzz} increase (decrease) under the compressive (tensile) strain, aligning with the polarization variation. Our work proposes shift current as a sensitive probe signal to detect mechanical deformation in piezoelectric systems.

Declarations The authors declare that they have no competing interests and there are no conflicts.

Electronic supplementary materials The online version contains supplementary material available at https://doi.org/10.15302/frontphys.2026.125204. See the supporting information for tight-binding model of 1D chain, derivation of the $k_1 - k_2$ constraint for simulating the negative and positive piezoelectric effect in the 1D chain model, the electronic structure of r-GeTe, the resolved shift current of Ge/Te atomic layer, the k-resolved shift current, k-resolved shift vector, and interband berry connection of r-GeTe of ±3% strain configurations, the in-plane shift current σ^{yyy} of r-GeTe under out-of-plane strain, the out-of-plane shift current σ^{zyy}, and σ^{zzz} of r-GeTe under in-plane strain, and the shift current of r-GeX (X = S, Se).

Acknowledgements We acknowledge the financial support from the National Natural Science Foundation of China (NSFC) under Grant Nos. 12274342 and 12374065 and the Young Talent Fund of Xi'an Association for Science and Technology. Additionally, the authors acknowledge support from Beijing PARATERA Technology Co., Ltd., for providing high-performance resources for contributing to the research results reported within this paper.

References

1. V. Belinicher, E. Ivchenko, and B. Sturman, Kinetic theory of the displacement photovoltaic effect in piezoelectrics, *Zh. Eksp. Teor. Fiz.* 56(2), 359 (1982)
2. J. E. Sipe and A. I. Shkrebtii, Second-order optical response in semiconductors, *Phys. Rev. B* 61(8), 5337 (2000)
3. N. Kristoffel, R. Von Baltz, and D. Hornung, On the intrinsic bulk photovoltaic effect: Performing the sum over intermediate states, *Z. Phys. B* 47(4), 293 (1982)
4. Y. Zhao, Q. Xue, X. Mu, H. Cui, and J. Zhou, Recent advances of bulk photovoltaic effect in exotic quantum materials: Progress and challenges, *Adv. Mater.* doi: 10.1002/adma.202517783 (2026)
5. B. M. Fregoso, Bulk photovoltaic effects in the presence of a static electric field, *Phys. Rev. B* 100(6), 064301 (2019)
6. B. I. Sturman, Ballistic and shift currents in the bulk photovoltaic effect theory, *Phys. Uspekhi* 63(4), 407 (2020)
7. C. Zhang, H. Pi, L. Zhou, S. Li, J. Zhou, A. Du, and H. Weng, Switchable topological phase transition and nonlinear optical properties in a ReC_2H monolayer, *Phys. Rev. B* 105(24), 245108 (2022)
8. Y. Gao, M. T. Yang, W. L. Zou, J. Zhou, and C. M. Zhang, Band-edge mixture engineered giant and switchable shift current generation, *Nano Lett.* 24(40), 12560 (2024)
9. C. M. Zhang, P. Guo, and J. Zhou, Tailoring bulk photovoltaic effects in magnetic sliding ferroelectric materials, *Nano Lett.* 22(23), 9297 (2022)
10. S. M. Young and A. M. Rappe, First principles calculation of the shift current photovoltaic effect in ferroelectrics, *Phys. Rev. Lett.* 109(11), 116601 (2012)
11. L. Z. Tan and A. M. Rappe, Enhancement of the bulk photovoltaic effect in topological insulators, *Phys. Rev. Lett.* 116(23), 237402 (2016)
12. M. M. Yang, D. J. Kim, and M. Alexe, Flexo-photovoltaic effect, *Science* 360(6391), 904 (2018)
13. N. Kristoffel, R. von Baltz, and D. Hornung, On the intrinsic bulk photovoltaic effect: Performing the sum over intermediate states, *Z. Phys. B* 47(4), 293 (1982)
14. Y. Li, J. Fu, X. Mao, C. Chen, H. Liu, M. Gong, and H. Zeng, Enhanced bulk photovoltaic effect in two-dimensional ferroelectric $CuInP_2S_6$, *Nat. Commun.* 12(10), 5896 (2021)
15. F. Xu, H. Su, Z. Gong, Y. Wei, H. Jin, and H. Guo, Controllable ferroelectricity and bulk photovoltaic effect in elemental group-V monolayers through strain engineering, *Phys. Rev. B* 106(19), 195418 (2022)
16. T. Rangel, B. M. Fregoso, B. S. Mendoza, T. Morimoto, J. E. Moore, and J. B. Neaton, Large bulk photovoltaic effect and spontaneous polarization of single-layer monochalcogenides, *Phys. Rev. Lett.* 119(6), 067402 (2017)
17. R. P. Tiwari, B. Birajdar, and R. K. Ghosh, First-principles calculation of shift current bulk photovoltaic effect in two-dimensional α-In_2Se_3, *Phys. Rev. B* 101(23), 235448 (2020)
18. J. Wei, Y. Li, L. Wang, W. Liao, B. Dong, C. Xu, C. Zhu, K. W. Ang, C. W. Qiu, and C. Lee, Zero-bias mid-infrared graphene photodetectors with bulk photoresponse and calibration-free polarization detection, *Nat. Commun.* 11(1), 6404 (2020)
19. M. Sotome, M. Nakamura, J. Fujioka, M. Ogino, Y. Kaneko, T. Morimoto, Y. Zhang, M. Kawasaki, N. Nagaosa, Y. Tokura, and N. Ogawa, Spectral dynamics of shift current in ferroelectric semiconductor SbSI, *Proc. Natl. Acad. Sci. USA* 116(6), 1929 (2019)
20. Y. J. Zhang, T. Ideue, M. Onga, F. Qin, R. Suzuki, A. Zak, R. Tenne, J. H. Smet, and Y. Iwasa, Enhanced intrinsic photovoltaic effect in tungsten disulfide nanotubes, *Nature* 570(7761), 349 (2019)
21. N. Setter, D. Damjanovic, L. Eng, G. Fox, S. Gevorgian, S. Hong, A. Kingon, H. Kohlstedt, N. Y. Park, G. B. Stephenson, I. Stolitchnov, A. K. Taganstev, D. V. Taylor, T. Yamada, and S. Streiffer, Ferroelectric thin films: Review of materials, properties, and applications, *J. Appl. Phys.* 100(5), 051606 (2006)
22. J. F. Scott, Applications of modern ferroelectrics, *Science* 315(5814), 954 (2007)
23. R. Nanae, S. Kitamura, Y. R. Chang, K. Kanahashi, T. Nishimura, R. Moqbel, K. H. Lin, M. Maruyama, Y. Gao, S. Okada, K. Qi, J. H. Fu, V. Tung, T. Taniguchi, K. Watanabe, and K. Nagashio, Bulk photovoltaic effect in single ferroelectric domain of SnS crystal and control of local polarization by strain, *Adv. Funct.*

Mater. 34(41), 2406140 (2024)
24. W. Wang, Y. Xiao, T. Li, X. Lu, N. Xu, and Y. Cao, Piezo-photovoltaic effect in monolayer 2H-MoS_2, *J. Phys. Chem. Lett.* 15(13), 3549 (2024)
25. Y. Dong, M. M. Yang, M. Yoshii, S. Matsuoka, S. Kitamura, T. Hasegawa, N. Ogawa, T. Morimoto, T. Ideue, and Y. Iwasa, Giant bulk piezophotovoltaic effect in 3R-MoS_2, *Nat. Nanotechnol.* 18(1), 36 (2023)
26. I. Katsouras, K. Asadi, M. Li, T. B. van Driel, K. S. Kjær, D. Zhao, T. Lenz, Y. Gu, P. W. M. Blom, D. Damjanovic, M. M. Nielsen, and D. M. de Leeuw, The negative piezoelectric effect of the ferroelectric polymer poly (vinylidene fluoride), *Nat. Mater.* 15(1), 78 (2016)
27. V. S. Bystrov, E. V. Paramonova, I. K. Bdikin, A. V. Bystrova, R. C. Pullar, and A. L. Kholkin, Molecular modeling of the piezoelectric effect in the ferroelectric polymer poly (vinylidene fluoride) (PVDF), *J. Mol. Model.* 19(9), 3591 (2013)
28. L. You, Y. Zhang, S. Zhou, A. Chaturvedi, S. A. Morris, F. Liu, L. Chang, D. Ichinose, H. Funakubo, W. Hu, T. Wu, Z. Liu, S. Dong, and J. Wang, Origin of giant negative piezoelectricity in a layered van der Waals ferroelectric, *Sci. Adv.* 5(4), eaav3780 (2019)
29. Y. Liu, W. Wang, Z. Wang, and C. Si, Ultrahigh negative longitudinal piezoelectricity in rhombohedral GeTe and its group IV–VI analogues, *Nano Lett.* 25(9), 3630 (2025)
30. Z. G. Wang, S. Shu, X. Wei, R. Liang, S. Ke, L. Shu, and G. Catalan, Flexophotovoltaic effect and above-band-gap photovoltage induced by strain gradients in halide perovskites, *Phys. Rev. Lett.* 132(8), 086902 (2024)
31. Z. Wang, H. Zhong, Z. Liu, X. Hu, L. Shu, and G. Catalan, Strain-gradient-induced modulation of photovoltaic efficiency, *Matter* 8(3), 101930 (2025)
32. G. Kresse and J. Furthmüller, Efficient iterative schemes for ab initio total-energy calculations using a plane-wave basis set, *Phys. Rev. B* 54(16), 11169 (1996)
33. J. P. Perdew, K. Burke, and M. Ernzerhof, Generalized gradient approximation made simple, *Phys. Rev. Lett.* 77(18), 3865 (1996)
34. G. Kresse and D. Joubert, From ultrasoft pseudopotentials to the projector augmented-wave method, *Phys. Rev. B* 59(3), 1758 (1999)
35. H. J. Monkhorst and J. D. Pack, Special points for Brillouin-zone integrations, *Phys. Rev. B* 13(12), 5188 (1976)
36. R. King-Smith and D. Vanderbilt, Theory of polarization of crystalline solids, *Phys. Rev. B* 47(3), 1651 (1993)
37. A. A. Mostofi, J. R. Yates, G. Pizzi, Y. S. Lee, I. Souza, D. Vanderbilt, and N. Marzari, An updated version of Wannier90: A tool for obtaining maximally-localised Wannier functions, *Comput. Phys. Commun.* 185(8), 2309 (2014)
38. A. A. Mostofi, J. R. Yates, Y. S. Lee, I. Souza, D. Vanderbilt, and N. Marzari, wannier90: A tool for obtaining maximally-localised Wannier functions, *Comput. Phys. Commun.* 178(9), 685 (2008)
39. W. P. Su, J. R. Schrieffer, and A. J. Heeger, Solitons in polyacetylene, *Phys. Rev. Lett.* 42(25), 1698 (1979)
40. J. E. Sipe and A. I. Shkrebtii, Second-order optical response in semiconductors, *Phys. Rev. B* 61(8), 5337 (2000)
41. J. Ibañez-Azpiroz, S. S. Tsirkin, and I. Souza, Ab initio calculation of the shift photocurrent by Wannier interpolation, *Phys. Rev. B* 97(24), 245143 (2018)
42. S. J. Gong, F. Zheng, and A. M. Rappe, Phonon influence on bulk photovoltaic effect in the ferroelectric semiconductor GeTe, *Phys. Rev. Lett.* 121(1), 017402 (2018)
43. R. P. Tiwari, Enhanced shift current bulk photovoltaic effect in ferroelectric Rashba semiconductor α-GeTe: ab initio study from three- to two-dimensional van der Waals layered structures, *J. Phys.: Condens. Matter* 34(43), 435404 (2022)
44. R. Fei, S. Yu, Y. Lu, L. Zhu, and L. Yang, Switchable enhanced spin photocurrent in Rashba and cubic Dresselhaus ferroelectric semiconductors, *Nano Lett.* 21(5), 2265 (2021)
45. M. Hong, W. Lyv, M. Li, S. Xu, Q. Sun, J. Zou, Z. G. Chen, Rashba effect maximizes thermoelectric performance of GeTe derivatives, *Joule* 4(9), 2030 (2020)
46. J. W. Park, S. H. Eom, H. Lee, J. L. Da Silva, Y. S. Kang, T. Y. Lee, and Y. H. Khang, Optical properties of pseudobinary GeTe, $Ge_2Sb_2Te_5$, $GeSb_2Te_4$, $GeSb_4Te_7$, and Sb_2Te_3 from ellipsometry and density functional theory, *Phys. Rev. B* 80(11), 115209 (2009)
47. J. Li, X. Zhang, Z. Chen, S. Lin, W. Li, J. Shen, I. T. Witting, A. Faghaninia, Y. Chen, A. Jain, L. Chen, G. J. Snyder, and Y. Pei, Low-symmetry rhombohedral GeTe thermoelectrics, *Joule* 2(5), 976 (2018)
48. D. Di Sante, P. Barone, R. Bertacco, and S. Picozzi, Electric control of the giant Rashba effect in bulk GeTe, *Adv. Mater.* 25(4), 509 (2013)
49. X. C. Mu, Q. Q. Xue, Y. Sun, and J. Zhou, Magnetic proximity enabled bulk photovoltaic effects in van der Waals heterostructures, *Phys. Rev. Res.* 5(1), 013001 (2023)
50. H. Zhou, R. C. Xiao, S. H. Zhang, W. Gan, H. Han, H. M. Zhao, W. Lu, C. Zhang, Y. Sun, H. Li, and D. F. Shao, Skin effect of nonlinear optical responses in antiferromagnets, *Phys. Rev. Lett.* 133(23), 236903 (2024)
51. S. M. Young, F. Zheng, and A. M. Rappe, First-principles calculation of the bulk photovoltaic effect in bismuth ferrite, *Phys. Rev. Lett.* 109(23), 236601 (2012)
52. S. M. Young and A. M. Rappe, First principles calculation of the shift current photovoltaic effect in ferroelectrics, *Phys. Rev. Lett.* 109(11), 116601 (2012)
53. S. Zhong, X. Zhang, S. Liu, S. A. Yang, and Y. Lu, Giant and nonanalytic negative piezoelectric response in elemental group-V ferroelectric monolayers, *Phys. Rev. Lett.* 131(23), 236801 (2023)
54. J. Yu, Y. Zhang, S. Yang, C. Song, S. Xu, B. Huang, Q. Wang, and J. Li, Self-powered tunable photodetection via flexoelectric engineering of single-phase 2H-MoS_2, *Materiomics* 11(6), 101103 (2025)